



# Quantitative quality-control metrics for *in vivo* oximetry in small vessels by visible light optical coherence tomography angiography

RONGRONG LIU,<sup>1</sup> WEIYE SONG,<sup>2</sup> VADIM BACKMAN,<sup>1</sup> AND JI YI<sup>2,\*</sup>

<sup>1</sup>Department of Biomedical Engineering, Northwestern University, Evanston, IL, 60208, USA

<sup>2</sup>Department of Medicine, Boston University School of Medicine, Boston, MA, 02118, USA

\*jiyi@bu.edu

**Abstract** Biological functions rely on local microvasculature to deliver oxygen and nutrients and carry away metabolic waste. Alterations to local oxygenation levels are manifested in diseases including cancer, diabetes mellitus, etc. The ability to quantify oxygen saturation ( $sO_2$ ) within microvasculature *in vivo* to assess local tissue oxygenation and metabolic function is highly sought after. Visible light optical coherence tomography (vis-OCT) angiography has shown promise in reaching this goal. However, achieving reliable measurements in small vessels can be challenging due to the reduced contrast and requires data averaging to improve the spectral data quality. Therefore, a method for quality-control of the vis-OCT data from small vessels becomes essential to reject unreliable readings. In this work, we present a quantitative metrics to evaluate the spectral data for a reliable measurement of  $sO_2$ , including angiography signal to noise ratio (SNR), spectral anomaly detection and discard, and theory-experiment correlation analysis. The thresholds for each quantity can be flexibly adjusted according to different applications and system performance. We used these metrics to measure  $sO_2$  of C57BL/6J mouse lower extremity microvasculature and validated it by introducing hyperoxia for expected  $sO_2$  changes. After validation, we applied this protocol on C57BL/6J mouse ear microvasculature to conduct *in vivo* small blood vessel OCT oximetry. This work seeks to standardize the data processing method for *in vivo* oximetry in small vessels by vis-OCT.

© 2019 Optical Society of America under the terms of the [OSA Open Access Publishing Agreement](#)

## 1. Introduction

Biological functions rely on local microvasculature to deliver oxygen and nutrients and carry away metabolic waste. In the local microvascular environment, oxygen unloads from hemoglobin and diffuses freely from RBCs to tissues following the gradient of oxygen partial pressure ( $pO_2$ ), and within the vessels  $pO_2$  determines the oxygen saturation ( $sO_2$ ) of RBC hemoglobin. Thus, a measurement of microvascular  $sO_2$  can indirectly assess local tissue oxygenation and metabolic function. Alterations to local oxygenation levels are manifested in diseases including cancer, diabetes mellitus, inflammatory processes, and so on [1–5]. In the case of tumor development and diabetes mellitus, angiogenesis is induced by local hypoxia and can be reflected by abnormal local oxygenation levels. Therefore, the ability to quantify  $sO_2$  in the small vessels *in vivo*, down to capillaries, is highly sought after. Because of its critical importance, several non-invasive and label-free methods have been developed. Near-infrared optical coherence tomography angiography (NIR OCTA) [6–10] and adaptive optics laser scanning ophthalmoscopy (AOLSO) [11–14] have been used to image capillaries, and single-RBC photoacoustic (PA) flowoxigraphy (FOG) [15] has been used to measure capillary  $sO_2$ . However, NIR OCTA and AOLSO are not able to measure  $sO_2$ , and PA FOG requires cumbersome mechanical contact. Recently, visible light optical coherence tomography (vis-OCT) angiography, a non-invasive backscattering-based imaging modality, has shown promise in measuring  $sO_2$  *in vivo* [16,17]. It has been successfully demonstrated in arteriolar-level vessels. Recent reports have shown that oximetry is also possible at capillary

level using vis-OCT combined with angiography-navigated microvascular signals, both theoretically [18] and experimentally [19]. Our results indicate that in order to obtain sufficient signal-to-noise ratio (SNR), and to smooth out the RBC geometry-dependent scattering, a temporal averaging on one single vessel or spatial averaging over a local capillary network is required. Because the process of averaging (e.g. how much data should be used for averaging) depends on the experimental conditions and imaging sites, a general data quality-control protocol is of instrumental importance.

In this work, we have proposed a quantitative data quality-control protocol to evaluate the data quality of vis-OCT angiography signals to measure  $sO_2$  from small vessels *in vivo*. This protocol includes the extraction of microvascular backscattering spectra measured by vis-OCT, a three-step statistical data-cleaning process of the spectra to reveal hemoglobin spectral contrast, and  $sO_2$  quantification via least-squares fitting. The three-step statistical data-cleaning process is key to this protocol to reject outliers and evaluate the data quality. It consists of 1) SNR analysis and sample size estimation, 2) anomaly detection and outlier removal, and 3) spectral fitting test. We used this protocol to measure  $sO_2$  of different-sized blood vessels of wild type C57BL/6J mouse lower extremity down the femoral artery and validated it by introducing hyperoxia to the mouse for expected changes in  $sO_2$  results. After validation, we applied this protocol on C57BL/6J mouse ear microvasculature to conduct *in vivo* OCT oximetry down to small blood vessels such as capillaries. This quantitative method is generally applicable since parameters of the scanning protocol and the threshold requirements in the three-step statistical data-cleaning process can be flexibly adjusted according to different applications and system performance. Thus, it seeks to standardize the data processing method for *in vivo* oximetry in small vessels by vis-OCT.

## 2. Methods and materials

### 2.1 Theoretical model for OCT spectra of blood vessels

As illustrated in Fig. 1(a), we express the depth-dependent OCT backscattering spectra of a blood vessel by [16,19,20]:

$$I(\lambda, z_0 + z) = I_0(\lambda)I_t(\lambda, z_0)\mu_b(\lambda)e^{-2\mu_t(\lambda)z} \quad (1)$$

where  $\lambda$  is the central wavelength of a spectral band,  $I_0(\lambda)$  is the source spectrum,  $I_t(\lambda, z_0)$  is the spectrum of tissues above the blood vessel with a thickness of  $z_0$ ,  $\mu_b(\lambda)$  is the backscattering coefficient of red blood cells (RBC) [18],  $z$  is the depth within the blood vessel, and  $\mu_t(\lambda)$  is the extinction coefficient of hemoglobin. We simplify  $\mu_t(\lambda)$  as:

$$\mu_t(\lambda) = a(g(\lambda)) * \mu_s(\lambda) + \mu_a(\lambda) \quad (2)$$

where  $a$  is a function of hemoglobin anisotropic factor  $g$  [21],  $\mu_s$  and  $\mu_a$  are the scattering and absorption coefficients of whole blood, respectively. After normalization to the spectra of the source and tissues above the blood vessel, the accumulated backscattered light from this blood vessel can be denoted by an integration over the vessel diameter,  $z_l$ , resulting in:

$$I_{\text{vessel}}(\lambda, z_l) = \int_0^{z_l} \frac{I(\lambda, z_0 + z)}{I_0(\lambda)I_t(\lambda, z_0)} dz = \int_0^{z_l} \mu_b(\lambda)e^{-2\mu_t(\lambda)z} dz = \frac{\mu_b(\lambda)}{2\mu_t(\lambda)} [1 - e^{-2\mu_t(\lambda)z_l}] \quad (3)$$

The spectra of  $\mu_b(\lambda)$ ,  $\mu_a(\lambda)$ ,  $\mu_s(\lambda)$ ,  $g$ , are provided by the literature [18,22] and thus  $I_{\text{vessel}}(\lambda, z_l)$ , corresponding to the vis-OCT measured spectrum of this blood vessel, can be theoretically predicted. This serves as the mathematical basis for spectral analysis in this study.

## 2.2 System setup

The system setup for vis-OCT used in this study was modified from our previous publication [23,24] and its schematic is shown in Fig. 1(b). The light source is a supercontinuum laser (SuperK, NKT, Denmark) providing a broad band illumination. Visible light under 650 nm was filtered out by a dichroic mirror (DM), polarized by a polarization beam splitter (PBS), and dispersed by a pair of identical prisms (P1, P2). A beam block (B) passed the green light from ~520 to 610 nm. The green light was reflected by the mirror (M1), redirected by a D-shaped mirror (DSM), focused by a  $f = 10$  mm lens (L1), and coupled into a single-mode 50/50 fiber coupler (OFC), with a numerical aperture (NA) of approximately 0.12. In the sample arm, the green light was first collimated by a  $f = 10$  mm lens (L3), and then was scanned across an objective (LSM03-VIS, Thorlabs) using two galvanometer scanning mirrors (GM1, GM2) to achieve pointwise scanning at the sample. Given the fiber NA = 0.12, the diameter of the illumination beam passing into the objective was ~2.41 mm, and the lateral resolution was ~11.68  $\mu\text{m}$  at 565 nm. Given the effective working length of the objective = 39 mm, the depth of focus was ~0.38 mm at 565 nm. The incident power on the sample was ~1.6 mW. The backscattered light from the sample returned into the interferometer and interfered with the light from the reference arm. In the reference arm, the reference beam was first polarized by a paddle polarization controller (PC, FPC020, Thorlabs), and then collimated by a  $f = 10$  mm lens (L2) and reflected by a mirror (M2). A variable neutral density filter (VNDF) and several BK7 glass plates (DC) were installed in the reference arm to attenuate the light and compensate for dispersion in the sample arm. The returning light was sent to a custom-made spectrometer, which consisted of a 1800 lp/mm transmission grating (Wasatch), a multi-elements  $f = 150$  mm lens (JML Optics), and a line scan camera (spL2048-140km, Basler). The spectrometer took the spectrum from 535 to 600 nm as in a conventional Fourier domain OCT configuration, giving an axial resolution of ~2.18  $\mu\text{m}$  in air. The line scan camera digitized the dispersed spectrum at a speed of 70 kHz, with 2048 pixels selected to output the spectrum, and the exposure time of the camera was 7  $\mu\text{s}$ . A custom-built LabVIEW program synchronized galvanometric mirror scanning with spectrometer acquisition.

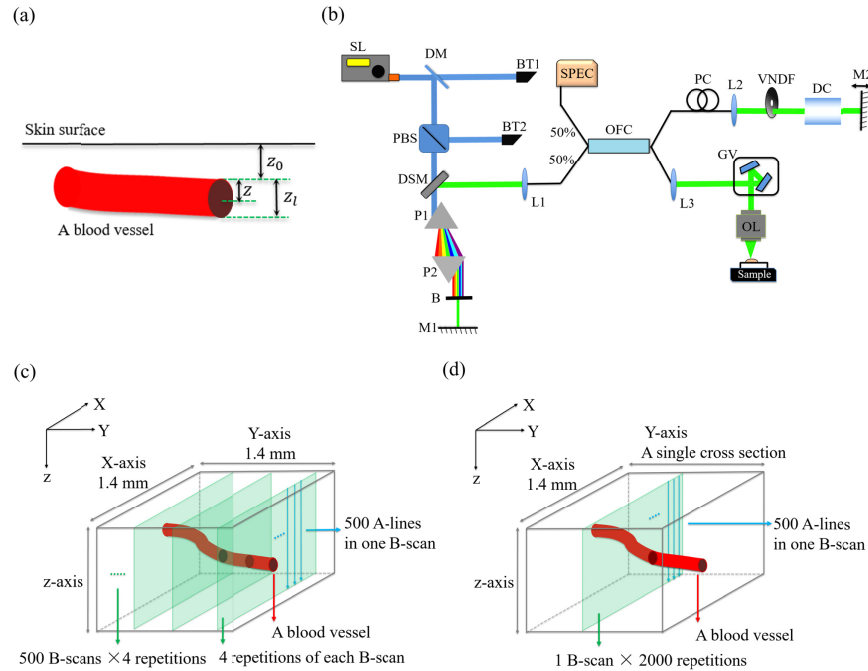


Fig. 1. Schematic and scanning protocols of the visible light spectroscopic optical coherence tomography (vis-OCT) imaging system. (a) Illustration of a blood vessel embedded in tissue. (b) Optical setup of vis-OCT. SL: supercontinuum source; DM: dichroic mirror; PBS: polarizing beam splitter; DSM: D-shaped mirror; P: prism; B: block; M: mirror; BT: beam trap; L: lens ( $f = 10$  mm); SPEC: spectrometer; OFC: wide band optical fiber coupler; PC: polarization controller; VNDf: variable neutral density filter; DC: dispersion control; GV: galvanometer mirror; OL: objective lens (Effective working length: 39 mm). (c) Illustration of scanning protocol 1. (d) Illustration of scanning protocol 2.

### 2.3 Animal preparation

All the experimental procedures were approved by the Boston University Institutional Animal Care and Use Committee (IACUC). We imaged the blood vessels of wild-type C57BL/6J mouse lower extremity down the femoral artery and the microvascular network of the ear. Before taking images, we initially anesthetized the mouse by inhalational anesthesia with 4.5% isoflurane for 10 minutes, followed by intraperitoneal anesthesia with 10% Ketamine/Xylazine cocktail solution (11.45 mg Ketamine and 1.71 mg Xylazine per ml of solution, respectively). The dosage was 87 mg Ketamine and 13 mg Xylazine per kilogram of body weight. The depilatory cream was applied to remove fur from the mouse leg and ear. For the leg, a small  $0.5 \times 0.5$  mm<sup>2</sup> incision was made to expose the blood vessels down the femoral artery [24]. The animal was placed onto a heating pad to maintain body temperature at 37 °C during the entire period of anesthesia. To introduce hyperoxia for increasing sO<sub>2</sub> of blood vessels, the animal was first ventilated with normal air (21% O<sub>2</sub>, 79% N<sub>2</sub>) at 4.2 Standard Liter per Minute (SLPM), and then was supplied with pure oxygen (100% O<sub>2</sub>). During both normal air and 100% O<sub>2</sub> ventilations, the animal was allowed to stabilize for at least 15 minutes before the measurements were taken. After the experiment, the mouse was allowed to recover and then sent back to the animal housing facility.

### 2.4 Scanning protocols

The backscattering signals from blood vessels were acquired with the spectrometer collecting 70,000 A-lines/sec at an exposure time of 7  $\mu$ s. Two scanning protocols were used during

data acquisition. The first scanning protocol is illustrated in Fig. 1(c). It covered a square field of view (FOV) of  $1.4 \times 1.4 \text{ mm}^2$  and was composed of repetitive ( $\times 4$ ) unidirectional B-scans of the same cross-section. Each B-scan consisted of 500 A-lines per repetition. A total of 500 B-scans  $\times$  4 repetitions was sequentially acquired to cover the full FOV. The second scanning protocol is illustrated in Fig. 1(d). It covered the same scanning length of 1.4 mm as the first one, but a total of 1 B-scan  $\times$  2000 repetitions was acquired from the same cross-section of the sample.

During data acquisition, we first used scanning protocol 1 to obtain spatial locations and sizes of blood vessels from their *en face* projection views; then for the same sample and same FOV, we selected a series of cross sections (B-scans) equally spaced in the *en face* projection view and used scanning protocol 2 to repetitively scan these cross sections for future averaging of signals from the same blood vessel sites.

### 2.5 Interferogram preprocessing and spectral calibration

Visible interferograms were preprocessed before doing vis-OCT spectral analysis [19]. The interferograms were first normalized to the reference arm intensity followed by direct current (DC) removal. The data was then resampled into k-space (wavenumber space,  $k = 2\pi / \lambda$ ) and digitally compensated for dispersion before short time Fourier transform (STFT). Visible spectral-dependent OCT A-lines,  $A(\lambda, z)$ , namely the magnitude of the complex results after STFT, were first squared and then normalized to a Rayleigh scattering reference medium and multiplied by a correcting factor of  $k^4$  to get  $I(\lambda, z_0 + z) / I_0(\lambda)$  in Eq. (1). Here  $\lambda$  is the center wavelength of the STFT Gaussian window,  $z_0$  is the thickness of tissue above the blood vessel,  $z$  is the depth within the blood vessel, and  $k$  is the wavenumber.

The Rayleigh scattering reference medium was prepared by diluting an 80 nm polystyrene latex bead solution (Molecular Probes by Life Technologies) to 4% w/v with deionized water. The refractive index of the polystyrene latex bead was 1.59. The bead solution was pipetted onto a glass slide before being scanned with vis-OCT. Normalized OCT spectra of beads were calculated by analyzing the vis-OCT signals from the top 65  $\mu\text{m}$  of beads.

### 2.6 Data processing for visible spectroscopic angiography

In conducting spectral analysis of blood vessels, we performed spectroscopic angiography to obtain the spectral profiles of blood vessels with motion-enhanced contrast [7]. The spectroscopic angiography enhanced the intensity of blood vessels with flow motion inside and diminished the intensity of static background tissues, which intrinsically increased the image SNR for spectral analysis.

To acquire spectroscopic angiography, a sweeping Gaussian window sampled the whole spectrum into twelve equally-spaced narrow bands in k-space. The swept wavelength range was 535 - 600 nm. Since angiography contrast originates from the decorrelation between repetitive B-scans due to blood cell movement, bulk sample movement must be mitigated to increase the contrast of blood vessels. To reduce the predominant bulk-motion noise in the axial dimension due to animal breath and heartbeat [25], the size of the sweeping Gaussian window we used was approximately  $0.2 \mu\text{m}^{-1}$ , relaxing the axial resolution to  $\sim 10.4 \mu\text{m}$  in tissue. This relaxation did not significantly sacrifice the blood flow signals, which were predominantly in the transverse dimension in microvasculature of mouse lower extremity and ear in this study. We also adopted a three-step approach to correct for the bulk sample movement for each Gaussian window swept STFT band [8]: 1) Four repetitive B-scans of the same cross-sectional area were co-registered according to their cross-correlation functions. 2) The axial global phase fluctuations between the four repetitive B-scans were corrected with two phase modifiers. 3) A 3D spectroscopic angiography was obtained by calculating the mean amplitude of differences between the four B-scans. After this three-step approach, all



3D spectroscopic angiographies were averaged across different STFT bands to reduce spectroscopic background noise for subsequent blood vessel segmentation.

### 2.7 Extracting vis-OCT spectra for sO<sub>2</sub> quantification

In 3D spectroscopic angiography of different STFT windows, a summation of intensities of all voxels within a blood vessel normalized by the source spectrum,  $I_0(\lambda)$ , and the spectrum

of tissue above this blood vessel,  $I_t(\lambda, z_0)$ , gives  $\frac{\sum_{z_l} I(\lambda, z_0 + z)}{I_0(\lambda)I_t(\lambda, z_0)}$ , corresponding to the aforementioned  $I_{\text{vessel}}(\lambda, z_l)$ . The source spectrum  $I_0(\lambda)$  could be easily recorded. To obtain  $I_t(\lambda, z_0)$ , we characterized the tissue above the blood vessel as a continuously varying refractive index medium, and approximated its spectrum as  $\lambda^\alpha$  under Rayleigh–Gans–Debye (RGD) scattering approximation [26, 27]. Thus  $\alpha$  could be estimated by least-squares fitting the vis-OCT measured spectrum of tissue above the blood vessel from the relationship  $I_t(\lambda, z_0) \propto \lambda^\alpha$ .

Besides normalization, extracting  $\frac{\sum_{z_l} I(\lambda, z_0 + z)}{I_0(\lambda)I_t(\lambda, z_0)}$  for sO<sub>2</sub> quantification involved segmentation and size measurement of blood vessels. First, a lateral region of interest (ROI) was manually drawn on the *en face* projective angiography to locate a single blood vessel, which would be shown as a horizontal stripe in the *en face* projective angiography of the data set acquired by scanning protocol 2. Then, a 3D ROI was generated by extruding the manually selected lateral ROI along depth, corresponding to a thickness of  $\sim 150 \mu\text{m}$  from the skin top surface. Next, the blood vessel was segmented from this 3D ROI for each angiographic band by conducting an intensity threshold-based algorithm on the 3D angiography averaging across different STFT windows. Finally, the size of the segmented vessel,  $z_l$ , was calculated by identifying the left and right vessel walls in the mean of the repetitive B-scans from the data set acquired by scanning protocol 2. With known vessel size, the theoretical  $I_{\text{vessel}}(\lambda, z_l)$  for the segmented blood vessel at oxygenated and deoxygenated states could be calculated as sO<sub>2</sub> calibration curves, denoted by  $I_{\text{vessel}}^O(\lambda, z_l)$  and  $I_{\text{vessel}}^D(\lambda, z_l)$ , respectively. Thus, the sO<sub>2</sub> of this blood vessel could be quantified by least-squares fitting the vis-OCT measured spectrum of the vessel to its sO<sub>2</sub> calibration curves.

### 2.8 Three-step statistical data-cleaning process of vis-OCT spectra

The three-step statistical data-cleaning process is key to the data quality-control protocol for *in vivo* vis-OCT oximetry in small vessels. This process was conducted on vis-OCT measured spectra of repetitive B-scans. As illustrated by the flow chart in Fig. 2, the three steps consist of 1) SNR analysis and sample size estimation, 2) anomaly detection and outlier removal, and 3) spectral fitting test.

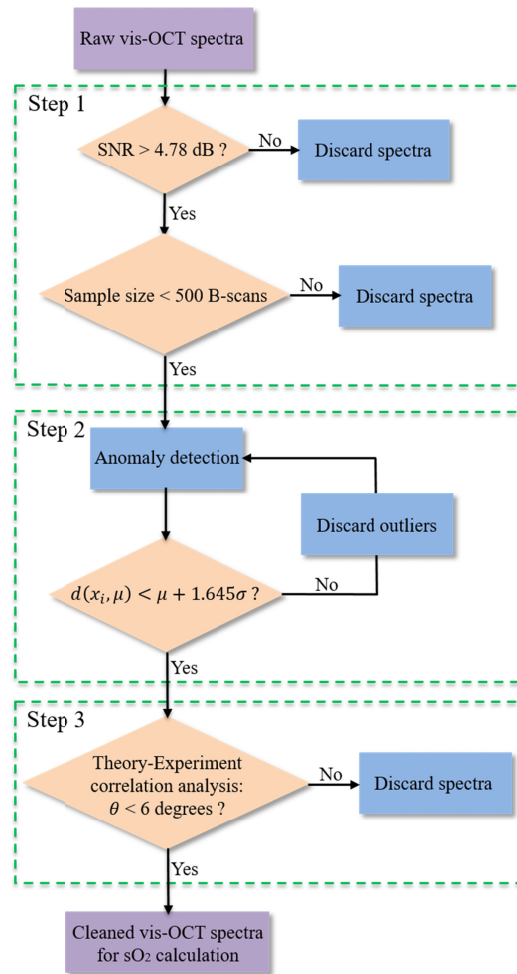


Fig. 2. Flow chart of the three-step statistical data-cleaning process of vis-OCT raw spectra. SNR: signal to noise ratio;  $x_i$ : the  $i^{\text{th}}$  spectrum of all repetitive spectra of a blood vessel;  $\mu$ : the mean spectra of all repetitive B-scans of a blood vessel;  $d(x_i, \mu)$ : the Mahalanobis distance (MD) between  $x_i$  and  $\mu$ ;  $\theta$ : the intersection angle between simulated and vis-OCT measured spectra of a blood vessel; sO<sub>2</sub>: oxygen saturation.

Step 1): SNR analysis and sample size estimation. In part 1, the SNR of spectroscopic angiography for each blood vessel was calculated. We defined SNR as  $\log_{10}(\mu_{\text{sig}} / \sigma_{\text{bg}})$  in dB scale for each B-scan, where  $\mu_{\text{sig}}$  is the mean intensity of signals within the blood vessel, and  $\sigma_{\text{bg}}$  is the standard deviation of intensities of the non-vascular background. We presented the spectroscopic SNR by the mean SNR of all repetitive B-scans for each angiographic band. Blood vessels with moderate SNR would be discarded from further analysis. We set a threshold for the mean SNR of spectroscopic angiography as 4.78 dB, corresponding to a mean vessel signal intensity three times the standard deviation of non-vascular background noise. In part 2, the minimum number of repetitive B-scans ( $N_{\text{mB}}$ ) needed to be averaged for extracting a reliable spectrum was estimated. In general, a blood vessel with a smaller  $N_{\text{mB}}$  indicated a smaller variation in spectra of all repetitive B-scans. To guarantee reliable measurements,  $N_{\text{mB}}$  of blood vessels should be smaller than the total number of B-scans that

the system acquires at each time. In our study, the total number of B-scans that our vis-OCT system could acquire for each acquisition was 500 B-scans, thus blood vessels with estimated  $N_{mB}$  more than 500 B-scans would be discarded from further analysis. To estimate  $N_{mB}$  for each blood vessel, we first divided spectra of all repetitive B-scans into training samples (spectra from the first 80% of B-scans), and validation samples (spectra from the last 20% of B-scans). Then, for each blood vessel, we calculated the mean of  $n$  randomly selected spectra from the training samples as  $\mu_n$ . Next, assuming that the training and validation samples had the same distribution, we calculated the mean of the Mahalanobis distance (MD) between each spectrum  $s_i$  from the validation samples and  $\mu_n$  as  $L(\mu_n)$ . Here the MD is defined as:

$$d(s_i, \mu_n) = \sqrt{(s_i - \mu_n)^T S^{-1} (s_i - \mu_n)} \quad (4)$$

where  $S$  is the covariance matrix of the  $n$  randomly selected spectra from the training samples; thus  $L(\mu_n)$  can be expressed by:

$$L(\mu_n) = \frac{1}{N_{val}} \sum_{i=1}^{N_{val}} d(s_i, \mu_n) \quad (5)$$

where  $N_{val}$  is the number of spectra in the validation samples. We iterated the above process (60 times) to obtain multiple  $L(\mu_n)$  for their mean as  $\overline{L(\mu_n)}$ , and standard deviation as  $\sigma_L$ . We define the coefficient of variation (CV) as  $\sigma_L / \overline{L(\mu_n)}$ . The  $N_{mB}$  is determined at the number where  $CV = 5\%$ .

Step 2): Anomaly detection and outlier removal. Spectra of blood vessels that passed SNR and  $N_{mB}$  checks in Step 1 might still contain abnormal spectra from a small number of B-scans, thus Step 2 focused on anomaly detection and outlier removal. For each blood vessel that passed Step 1, we first calculated the mean and variance of all repetitive B-scans as  $\mu$  and  $\sigma$ , respectively. Then we calculated the MD between each spectrum  $x_i$  and  $\mu$  as  $d(x_i, \mu)$ . Next, we set a threshold  $\hat{d} = \mu + 1.645\sigma$ , corresponding to a 95% confidence interval of Gaussian distribution, and discarded outliers, which were defined as  $d(x_i, \mu) > \hat{d}$ . We iterated this process until there were no outliers to discard, and afterward used the mean of the remaining spectra to quantify sO<sub>2</sub>.

Step 3): Spectral fitting test. Although we could quantify sO<sub>2</sub> from spectra of blood vessels that passed Step 1 and were processed by Step 2, it was still possible that the spectra extracted from spectroscopic angiography came from non-vascular tissues with unexpected motions. To remove such false measurements, Step 3 assessed the correlation between the measured and theoretically fitted spectra of blood vessels. Specifically, for each blood vessel with sO<sub>2</sub> quantified by least-squares fitting its calibration curves  $I_{vessel}^O(\lambda, z_l)$  and  $I_{vessel}^D(\lambda, z_l)$ , we could have an sO<sub>2</sub> fitted spectrum  $I_{fit}$  as:

$$I_{fit} = sO_2 \times I_{vessel}^O(\lambda, z_l) + (1 - sO_2) \times I_{vessel}^D(\lambda, z_l) \quad (6)$$

We calculated the intersection angle,  $\theta$ , between  $I_{fit}$  and the corresponding vis-OCT measured spectrum,  $\mu$ , from Step 2 to assess the correlation between theoretical prediction and measurement. Here we defined the intersection angle  $\theta$  as:



$$\theta = \cos^{-1} \left| \frac{I_{fit} \cdot \mu}{|I_{fit}| \cdot |\mu|} \right| \quad (7)$$

Spectra of blood vessels with weak correlation to theoretical predications would be removed as false measurements, even though they passed Step 1 and were processed by Step 2 for  $sO_2$  calculation. We set a threshold for the intersection angle  $\theta$  between measured and  $sO_2$  fitted OCT spectra as 6 degrees; thus blood vessels with  $\theta$  smaller than 6 degrees were discarded.

### 2.9 Reconstruction of *en face* $sO_2$ map

The 2D  $sO_2$  map on an *en face* OCT angiography was reconstructed by extracting the statistical expected  $sO_2$  of blood vessels within the imaging FOV. Essentially, the statistical expected  $sO_2$  of a blood vessel was calculated from the mean of signals from one or several given cross sections of the blood vessel over a certain period of time. This statistical result is more reliable to assess local tissue oxygenation than the  $sO_2$  of individual RBCs from any certain regions of a blood vessel at a certain time point, thus we used it to present the  $sO_2$  of a whole vessel segment. Although in local physiological environments, there exists heterogeneous oxygen partial pressure and thus  $sO_2$  within a single blood vessel [28], our primary interest is a confident measurement of  $sO_2$  averaged over time at one or several given locations of a blood vessel. Based on this and the aforementioned statistical data-cleaning process, an *en face*  $sO_2$  map could be reconstructed with a series of repetitive B-scans equally spaced on the *en face* OCT angiography to cover cross sections of most blood vessels for their statistical expected  $sO_2$ .

### 3. Results

#### 3.1 Data quality-control of vis-OCT spectra for $sO_2$ calculation

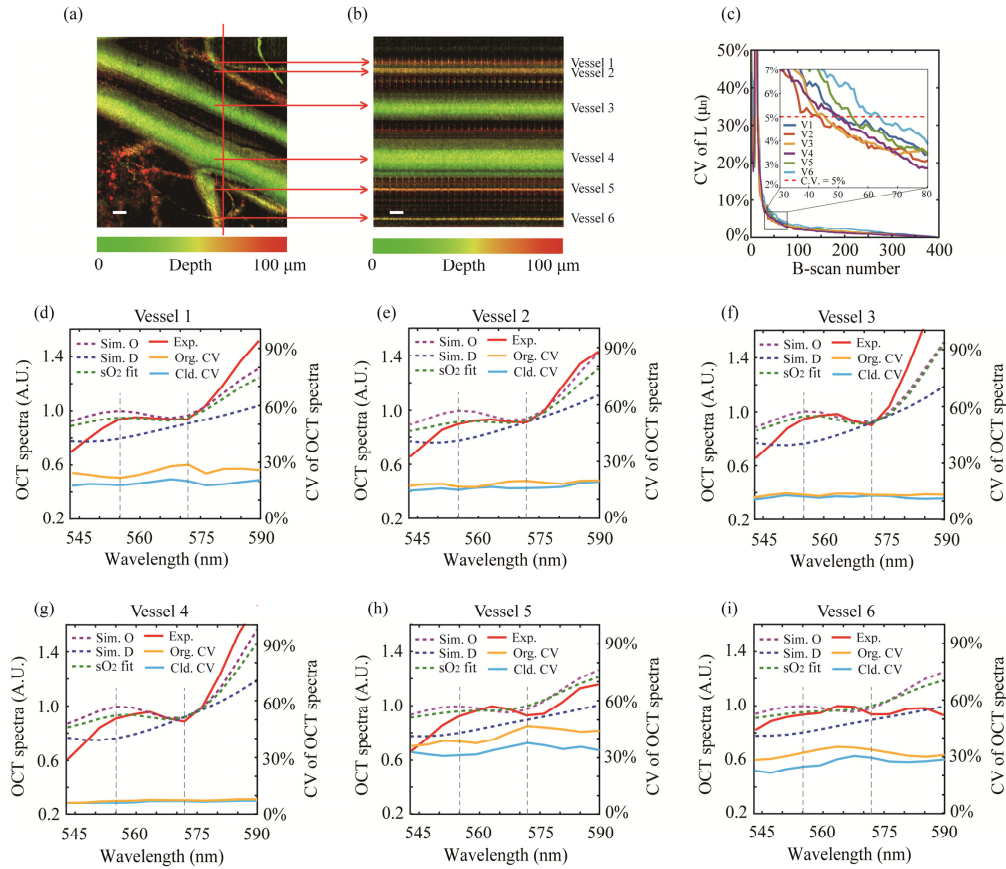


Fig. 3. Data quality control of vis-OCT spectra from six different sized blood vessels. (a) The *en face* angiography of wild-type C57BL/6J mouse lower extremity microvasculature acquired by scanning protocol 1. The red vertical line marks the location of a B-scan to be repetitively scanned. (b) The *en face* angiography of the marked B-scan in (a) acquired by scanning protocol 2. The color bar encodes depth locations of vessel central axis within 100  $\mu m$  from sample top surface. Scale bar: 100  $\mu m$ . Correspondence to the same blood vessels shown in (a) and (b) is indicated by red arrows in between. Blood vessels are numbered as Vessel 1, Vessel 2, Vessel 3, Vessel 4, Vessel 5, and Vessel 6, respectively. (c) The CV of  $L(\mu m)$ , the mean MD between the validation samples and randomly selected training samples, for six vessels, respectively. V1 - V6: Vessel 1 to Vessel 6. The red dashed line indicates CV = 5%. The black box zooms in on the region where CVs are around 5%. (d) – (i) The vis-OCT measured spectra processed by the data-cleaning and their corresponding simulated oxygenated, deoxygenated, and  $sO_2$  fitted spectra for V1 to V6, respectively. Simulated spectra are normalized by the maximum of oxygenated spectra within 555 – 572 nm, indicated by black vertical dashed lines; vis-OCT measured spectra are scaled to have the same mean as  $sO_2$  fitted spectra. Sim. O/D: simulated oxygenated/deoxygenated spectra; Exp.: Experimental measurements;  $sO_2$  fit:  $sO_2$  fitted spectra; Org./Cld CV: the coefficients of variation (CV) of the averaging OCT spectra before (original) and after (cleaned) the data-cleaning process. CV = S.D./Mean.

Table 1. Parameters of blood vessels and their  $sO_2$ 

Vessels	V1	V2	V3	V4	V5	V6
$D(\mu m)$	20.8	38.6	105.7	130.6	15.4	13.7
$\overline{SNR}(dB)$	7.2304	7.9394	7.9653	8.0752	8.8426	6.0468
$N_{mB}$	49	44	46	51	55	64
$N_{aB}$	332	374	366	405	203	225
$sO_2$	75.2%	62.6%	87.3%	73.1%	51.4%	45.3%
$\theta(\text{degree})$	0.665	0.908	1.52	1.57	2.03	1.97

To conduct *in vivo* vis-OCT oximetry, we imaged blood vessels with different sizes of the wild-type C57BL/6J mouse lower extremity down the femoral artery and used the data quality-control protocol to quantify  $sO_2$  from OCT spectra. An *en face* angiography acquired by scanning protocol 1 is shown in Fig. 3(a), where there are two major blood vessels, an arteriole and a venule, and other smaller blood vessels. Their diameters  $D$  are listed in Table 1. We continuously scanned one B-scan location for 14.2 seconds by scanning protocol 2, intersecting several vessels, with its *en face* angiography shown in Fig. 3(b). For simplicity, we number the six different vessels from top to bottom as vessel 1 to vessel 6, respectively. To do the aforementioned data-cleaning process, we first calculated the spectroscopic angiographic SNR for vessel 1 to vessel 6, respectively. The SNR analysis took less than 30 seconds for each blood vessel. The mean spectroscopic angiographic SNR for vessel 1 to vessel 6 are listed in Table 1. All of them are higher than the preset threshold 4.78 dB, corresponding to a mean vessel signal intensity three times the standard deviation of non-vascular background noise. We then checked  $N_{mB}$  of vessel 1 to vessel 6, respectively. We separated the total 500 B-scans into training samples (the first 400 B-scans) and validation samples (the last 100 B-scans). The CV of  $L(\mu_n)$ , the mean MD between the validation samples and randomly selected training samples, is shown in Fig. 3(c) for vessel 1 to vessel 6, respectively. The  $N_{mB}$  for vessel 1 to vessel 6 were calculated according to the threshold for CV of MD as 5%, indicated by a red dashed line. The black box in Fig. 3(c) zooms in on the region containing the starting points where CVs of MD are less than 5%. Estimating minimum B-scan numbers for measurement reliability took approximately 1 min for each blood vessel. The  $N_{mB}$  for vessel 1 to vessel 6 are listed in Table 1, demonstrating that approximately 60 B-scans were needed for spectral analysis of C57BL/6J mouse lower extremity angiography signals measured by our vis-OCT. This indicated that a total of 500 B-scans of the vessel cross section was far more than enough, ensuring measurement reliability in this study. Next, we extracted vis-OCT measured spectra of vessel 1 to vessel 6 and conducted anomaly detection to calculate their mean spectra, shown in Figs. 3(d)-3(i), respectively. To illustrate how the anomaly detection and outlier removal process works on a single blood vessel, scatter plots of the MD of vessel 1 with corresponding thresholds at each iteration of the process are shown in Appendix Fig. 7. The number of repetitive B-scans detected as normal versus iteration time for vessel 1 to vessel 6 are shown in Appendix Fig. 8, respectively. This process was iterated until there were no outliers to discard, and the number of repetitive B-scans remained after finishing this process, defined as  $N_{aB}$ , are listed in Table 1 for vessel 1 to vessel 6. The anomaly detection process took approximately 3 seconds for each blood vessel. Next, we extracted vis-OCT measured spectra of vessel 1 to vessel 6 and show them in Figs. 3(d)-3(i), respectively. According to the vessel diameters listed in Table 1, the vis-OCT spectra were simulated at oxygenated and deoxygenated states as calibration curves, shown in Figs. 3(d)-3(i) for each blood vessel. The  $sO_2$  of vessel 1 to vessel 6 were quantified by least-squares fitting their own calibration curves, listed in Table 1. The

wavelength range for  $sO_2$  calculation was from 555 to 572 nm, indicated by pairs of vertical dashed lines in Figs. 3(d)-3(i), because spectra at this range are most sensitive to oxygenation changes. Finally, to remove false measurements, we also show the  $sO_2$  fitted OCT spectra in Figs. 3(d)-3(i) and calculated the intersection angle between measured and  $sO_2$  fitted OCT spectra, listed in Table 1. The similarity analysis took approximately 1.5 seconds for each blood vessel. All vessels have intersection angles,  $\theta$ , less than 3 degrees, demonstrating the reliability of measurements from blood vessels. For comparison, the CV of vis-OCT measured spectra for vessel 1 to vessel 6 before and after the quality control process are shown in Figs. 3(d)-3(i). We can see that the original vis-OCT measured spectra display greater variations especially for vessel 1, vessel 2, vessel 5, and vessel 6. This indicates the significance of the statistical data-cleaning process for small blood vessels.

### 3.2 Validation of the data quality-control protocol for *in vivo* vis-OCT oximetry

After demonstrating *in vivo* vis-OCT oximetry with the data quality-control protocol, we next validated this protocol by a hyperoxia experiment. For normal air conditions, after acquiring the *en face* angiography in Fig. 3(a), we selected five B-scans equally-spaced on this *en face* view and repetitively scanned them to quantify  $sO_2$  of blood vessels crossed by these B-scans. For hyperoxia condition, we ventilated the mouse with 100% oxygen and acquired the data sets the same way as normal air condition. The *en face* angiography of the same scanning site at normal and 100% oxygen conditions are shown in Figs. 4(a) and 4(b), respectively. Before conducting the three-step statistical data-cleaning process, we first characterized the blood vessel sizes. Diameters of the same vessel measured from multiple cross sections were calculated as their mean, followed by standard deviations. During the data-cleaning process, we used the same thresholds as in Fig. 2 to ensure measurement traceability. Blood vessels with mean SNR lower than 4.78 dB were discarded from subsequent  $sO_2$  quantification. The  $N_{mb}$  of blood vessels marked in Fig. 4 after 100% oxygen ventilation fell in a range similar to those in Fig. 3(a), thus also much smaller than the total B-scan number (500 B-scans) that the vis-OCT could acquire at each time. With known vessel size, we quantified  $sO_2$  of each blood vessel via least-squares fitting the measured spectra to their corresponding theoretical calibration curves. Finally, we set a threshold for the intersection angle  $\theta$  between measured and  $sO_2$  fitted OCT spectra as 6 degrees, and blood vessels with  $\theta$  smaller than 6 degrees were discarded as false measurements. We marked the remaining blood vessels, including an arteriole, a venule, and other smaller blood vessels, by A, V, and numbers 3 to 9 in Figs. 4(a) and 4(b), respectively. There is a decrease in vessel size for most blood vessels after supplying 100%  $O_2$ , due to vasoconstriction. Figure 4(c) shows vessel diameters for A, V, and vessels 3 - 9 at normal and 100% oxygen conditions in descending order. Sizes of A, V, and V8 were measured from more than one data set, thus results are shown as their mean with standard deviations. We calculated statistical expected  $sO_2$  of blood vessels to assess local oxygenation levels as explained in section 2.9, thus vessel  $sO_2$  quantified from more than one data set were calculated as their mean. The quantified  $sO_2$  of these blood vessels at normal and 100% oxygen conditions are shown in Fig. 4(d). Most vessels, including A, V, and small vessels 4 and 6, show a significant increase in  $sO_2$ , with only V8 showing a decrease. We did a paired student t-test on these  $sO_2$  results, with a  $p$  value less than 0.01, indicating a significant  $sO_2$  increase after 100% oxygen ventilation. As a comparison, we also quantified  $sO_2$  of blood vessels in Fig. 3 from their original OCT spectra without any data-quality control process and show their  $sO_2$  histograms before and after data-quality control in Appendix Fig. 9. Although there is a similar increasing tendency in  $sO_2$  results, without quality control, some blood vessels display  $sO_2$  lower than 35%, and nearly all blood vessels had their  $sO_2$  increased to higher than 80% after oxygen ventilation. The abnormally low  $sO_2$  at normal air status and a globally significant  $sO_2$  increase in response to hyperoxia were unlikely to appear in mouse lower extremity blood vessels down to the capillary level.

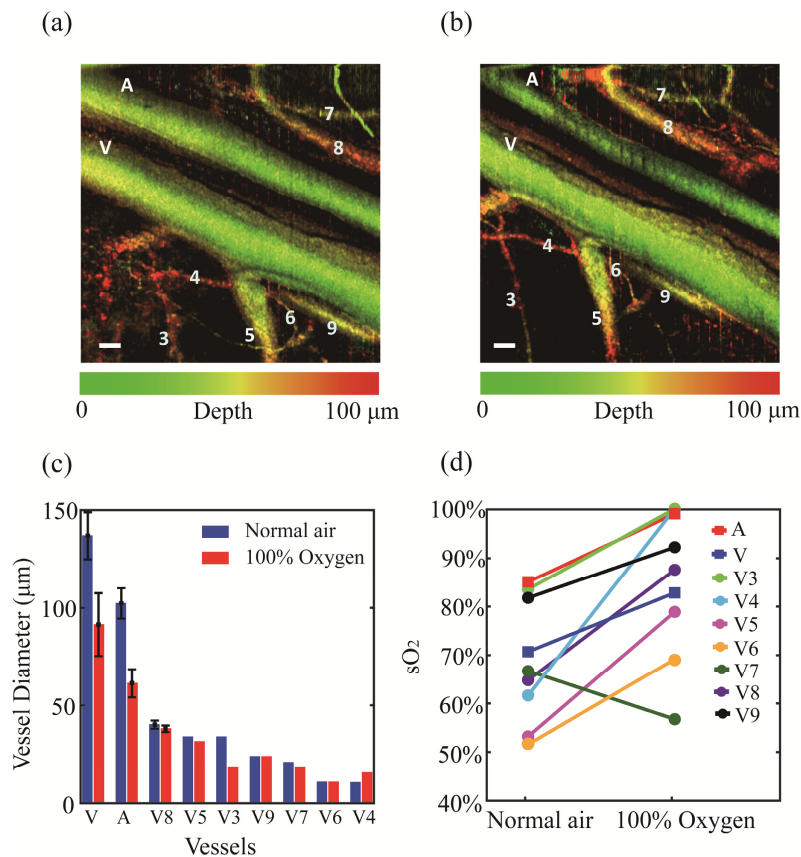


Fig. 4. Validation of the data quality-control protocol for *in vivo* vis-OCT Oximetry by supplying normal air and 100% oxygen to a wild-type C57BL/6J mouse. (a) The *en face* angiography of the mouse lower extremity microvasculature at normal air condition. (b) The *en face* angiography of the same imaging site in (a) ventilated by 100% pure oxygen. In (a) and (b), A: arteriole; V: venule; 3-9: vessel 3 to vessel 9. The color bar encodes depth of vessel central axis within 100  $\mu\text{m}$  from sample top surface. Scale bar: 100  $\mu\text{m}$ . (c) The sizes of blood vessels in (a) and (b) at normal and 100% oxygen conditions in descending order. (d) The quantified  $s\text{O}_2$  of blood vessels in (a) and (b) at normal and 100% oxygen conditions, respectively. In (c) and (d), A: arteriole; V: venule; V3 – V9: vessel 3 to vessel 9.

### 3.3 Demonstration of *in vivo* vis-OCT oximetry imaging

After validating the data quality-control protocol for *in vivo* vis-OCT optical oximetry by introducing hyperoxia, we applied our protocol to measure  $s\text{O}_2$  of C57BL/6J mouse ear microvasculature rich with small blood vessels at normal air condition. The melanin-containing skin of C57BL/6J mouse ear provided intrinsic noise to test the data quality-control protocol. After acquiring the *en face* angiography, we selected eleven B-scans equally-spaced on the *en face* view and repetitively scanned each of them to quantify  $s\text{O}_2$  of crisscrossed blood vessels. The crossed blood vessels were identified manually from the *en face* angiography according to positions of the eleven B-scans. We used the same thresholds as in Fig. 2 to ensure measurement traceability. Blood vessels with measurements not satisfying any of the threshold requirements were discarded as unreliable or false measurements. We also calculated statistical expected  $s\text{O}_2$  of blood vessels to assess local oxygenation levels as explained in section 2.9, and vessels with  $s\text{O}_2$  quantified from multiple cross sections were calculated as their mean. Based on this, we reconstructed a 2D *en face*  $s\text{O}_2$  map for mouse ear microvasculature, shown in Fig. 5. The angiography image quality is



inferior to the lower extremity microvasculature in Fig. 4(a) and 4(b), due to reduced light penetration by C57BL/6J mouse ear skin melanin, but the  $sO_2$  map still displays local oxygenation trend. Two blue arrows indicate locations of a pair of arteriole (A) and venule (V), with quantified  $sO_2$  of approximately 100% and 60%, respectively, which self-verified our measurement. Furthermore,  $sO_2$  of most small blood vessels (10-20  $\mu m$ ) could still be quantified. Even if RBCs may pass in a single file and in a discrete pattern in small blood vessels down to capillaries, leaving certain regions within small blood vessels to lose signals from RBCs at times, our spectral analysis for  $sO_2$  calculation was based on angiography signals, which inherently excluded signals from regions without blood motion. As a comparison, we also show the same  $sO_2$  map as in Fig. 5 but without any data quality control process in Appendix Fig. 10. Although the arteriole and venule show similar  $sO_2$  results, without quality-control, significant non-vascular signals were not rejected as false  $sO_2$  results, and most small blood vessels display  $sO_2$  either too close to 100% or lower than 30%, which appears physiologically unlikely. These demonstrate the feasibility of vis-OCT to do *in vivo* microvascular oximetry.

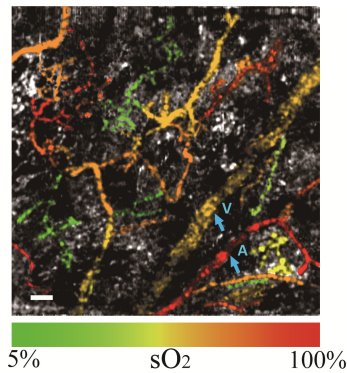


Fig. 5. The *en face*  $sO_2$  map of C57BL/6J mouse ear microvasculature. The blue arrows indicate locations of the arteriole and the venule. A: arteriole; V: venule. Scale bar: 100  $\mu m$ .

#### 4. Discussion

We proposed a quantitative data quality-control protocol to conduct reliable *in vivo* vis-OCT oximetry in small blood vessels. Briefly, as key to this protocol, a three-step statistical data-cleaning process cleaned up the raw backscattering spectra of microvasculature measured by vis-OCT to better reveal hemoglobin spectral contrast for reliable  $sO_2$  quantification. The three steps consist of SNR analysis and sample size estimation, anomaly detection and outlier removal, and spectral fitting test. We used this quantitative data quality-control protocol to measure  $sO_2$  of different-sized blood vessels of wild-type C57BL/6J mouse lower extremity down the femoral artery and validated it by introducing hyperoxia for expected  $sO_2$  changes. After validation, we applied this protocol on C57BL/6J mouse ear microvasculature to conduct *in vivo* small blood vessel OCT oximetry. This quantitative data quality-control protocol is generally applicable since parameters of the scanning protocol and the threshold requirements can be flexibly adjusted according to different applications and system performance.

The oxygenation contrast of a blood vessel's OCT spectra at oxygenated and deoxygenated states is affected by vessel size, thus characterizing vessel size is an essential prerequisite for  $sO_2$  quantification. As presented in Eq. (3),  $I_{vessel}(\lambda, z_l)$  is essentially the accumulated backscattered light from the blood vessel, and it was simulated by integrating OCT signal intensities over the vessel diameter,  $z_l$ . To explore the effect of vessel diameter on OCT spectra, we simulated OCT spectra of blood vessels with different diameters ranging



from capillary ( $\sim 10\text{--}15\ \mu\text{m}$ ) to major arteriole and venule ( $70\text{--}150\ \mu\text{m}$ ) by the equations in section 2.1. As shown in Fig. 6, the red and blue colors indicate spectra of oxygenated and deoxygenated states of the blood vessel, respectively. Larger size of blood vessels indicates greater magnitude and contrast between the oxygenated and deoxygenated states. When the vessel diameter is greater than  $70\ \mu\text{m}$ , both the magnitude and contrast of OCT spectra do not significantly increase. For example, spectra of  $70\ \mu\text{m}$  and  $150\ \mu\text{m}$  blood vessels are quite close, and their simulations of the same oxygen state almost overlap with each other. This is due to the depth-dependent attenuation of light. Since the measured and simulated OCT spectra in this study are accumulated backscattering signals within blood vessels, signals from superficial regions of vessel are less attenuated; as the vessel size increases, backscattering signals from superficial regions of the vessel will gradually dominate the accumulated spectra of the whole vessel. Therefore, the size measurement of blood vessels is necessary to  $\text{sO}_2$  quantification in this study.

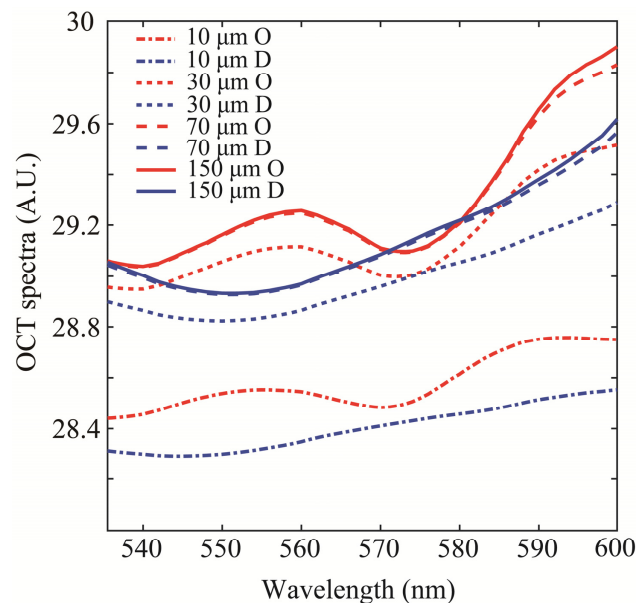


Fig. 6. Simulation results of OCT spectra in log scale for oxygenated and deoxygenated blood vessels with diameters of  $10\ \mu\text{m}$ ,  $30\ \mu\text{m}$ ,  $70\ \mu\text{m}$ , and  $150\ \mu\text{m}$ , respectively. O: oxygenated state; D: deoxygenated state.

In  $\text{sO}_2$  calculations, although a spectral range from 520 nm to 585 nm has been used to assess  $\text{sO}_2$  in previous work [29,30], we performed spectral fitting within a narrow range, 555–572 nm, instead of the full spectral range of our vis-OCT system, approximately 543–590 nm, due to several considerations. First, as shown in Figs. 3(d) – 3(i), oxygenated and deoxygenated blood have the best spectral contrast with opposite trends within the narrow range. Although in principle a broader spectrum includes more information, in experiments the fitting error actually increased at wavelengths beyond the range of 550–580 nm, and this was particularly prominent in small vessels. A narrower range could exclude those regions with undesired spectral deviations. Second, for all six blood vessels in Fig. 3, we noticed a decrease in the image SNR of angiography at wavelengths higher than 575 nm, as shown in Appendix Fig. 11 for all six blood vessels in Fig. 3. We attributed this SNR deterioration to increased penetration of light in non-vascular background tissues, which possibly led to a higher level of background signal. A narrower spectral range of 555–572 nm could avoid low SNR at longer wavelengths above 575 nm. To quantitatively ensure that limiting the spectral band to 555–572 nm would have comparable performance to a wider band, we conducted

similarity analysis between simulated OCT spectra with and without different zero-mean Gaussian white noise at three different spectra bands: 546-584 nm, 549-578 nm, and 552-572 nm. The standard deviations ( $\sigma_G$ ) of the added Gaussian noise were 10%, 5%, and 2% of the mean of the simulated noiseless spectra ( $\mu$ ), simulating systems with low, medium, and high performance. Appendix Fig. 12(a) to 12(d) show that when added by the same zero-mean Gaussian noise (with equal  $\sigma_G$ ), simulations with and without noise at  $sO_2$  of 60%, 70%, 80%, and 90% have quite close intersection angles, not only among different spectral bands, but also among vessels with diameters ranging from 10 to 150  $\mu m$ . These demonstrate the feasibility of using spectra from 555 to 572 nm for  $sO_2$  calculations to reduce errors caused by spectral deviations or SNR deterioration at both ends of the whole spectrum.

The 3-step statistical data quality-control process especially improved  $sO_2$  measurements for small blood vessels. The comparison between original and quality-controlled  $sO_2$  of mouse lower extremity blood vessels (in Fig. 4 and Appendix Fig. 9) and ear microvasculature (in Fig. 5 and Appendix Fig. 10) show that the quality-control process could effectively reject false  $sO_2$  results caused by noise from non-vascular background tissues and gave more reasonable  $sO_2$  values for vessels down to the capillary level. Furthermore, after the process, the spectral variations decreased, particularly for small blood vessels. Intrinsically, without quality-control, the vis-OCT measured spectra of smaller blood vessels have higher standard deviations between spectra of repetitive B-scans, and for blood vessels with sizes of  $\sim 10 \mu m$ , the original spectral CV are up to 30% - 45%, as shown in Fig. 3(h) and 3(i), respectively. This is because in small capillary-sized blood vessels, RBCs with different orientations and sizes discretely pass through in single file, leading to oscillatory backscattering spectra for each repetitive B-scan; however, the mean spectra after averaging can reveal the oxygenation contrast for  $sO_2$  calculation, as demonstrated in our previous work [18]. On the other side, for larger blood vessels, such as the arteriole, the venule, and a medium-sized blood vessel, as shown in Figs. 3(e), 3(f), and 3(g), their spectral CV after the data quality-control process only moderately improved, due to a stronger spectral contrast as shown in Fig. 6.

The thresholds for image SNR, the minimum repetitive B-scan number for a reliable measurement,  $N_{mB}$ , and the intersection angle between measurement and prediction,  $\theta$ , were determined according to the following criteria: For the SNR threshold for vis-OCT angiography images, it was determined as 4.78 dB, corresponding to a mean vessel signal intensity three times the standard deviation of the non-vascular background signal. For the threshold of  $N_{mB}$  to acquire a reliable  $sO_2$  quantification by, but not limited to, our vis-OCT system it was determined as when the CV of  $L(\mu_n)$  equals 5%, as explained in section 2.8. For the threshold of  $\theta$ , we set it as 6 degrees. This value was estimated according to the intersection angles between simulated spectra of blood vessels with  $sO_2 = \alpha$ , and with  $sO_2 = \alpha \pm 5\%$  added by a zero-mean Gaussian white noise. We allowed an error of 5% according to previous  $sO_2$  measurements by vis-OCT, which had standard deviations as 6.4% and 7.4% or lower for retinal arterioles and venules, respectively [8,16]. We assumed different standard deviations ( $\sigma_G$ ) of the zero-mean Gaussian white noise as 10%, 5% and 2% of the mean ( $\mu$ ) of the simulated spectrum with  $sO_2 = \alpha$ , respectively, to simulate imaging systems with low, medium, and high performance. In the case of the lowest system performance, where  $\sigma_G = 10\% \mu$ ,  $\theta$  for blood vessels with diameters ranging from 10 to 150  $\mu m$  and with  $sO_2$  of  $60\% \pm 5\%$ ,  $75\% \pm 5\%$ , and  $90\% \pm 5\%$  added by the Gaussian noise with the highest standard deviation are approximately upper bounded by 6 degrees, as shown in Appendix Figs. 13(a)-13(c), respectively. Thus, we determined the  $\theta$  threshold as 6 degrees, ensuring the  $sO_2$  measurement sensitivity to be approximately within the range of 5% at the lowest performance of the imaging system. However, in a different system with better performance,

the  $\theta$  threshold can be much lower than 6 degrees to ensure the  $\sim \pm 5\%$  accuracy. For example, as in Appendix Fig. 13, when the added Gaussian noise had lower variations, where  $\sigma_G = 5\%\mu$  and  $\sigma_G = 2\%\mu$ , the  $\theta$  thresholds can be  $\sim 3$  degrees and  $\sim 1.2$  degrees, respectively. As a whole, with our vis-OCT system and scanning protocols described in 2.2 and 2.4, respectively, all the aforementioned thresholds worked reasonably well in imaging mouse lower extremity and ear microvasculature. In future experiments, the thresholds in those metrics are subject to change depending on the imaging system and applications. For example, the image SNR threshold can be adjusted according to different requirements for imaging quality, and the  $\theta$  threshold can be smaller for the same imaging system if higher precision of  $sO_2$  measurements is desired. Generally speaking, a stricter threshold criterion indicates a more reliable measurement towards  $sO_2$ , but with higher requirements for image quality and measurement precision.

In determining the value of  $N_{mB}$  we used repeated B-scans at the same location, and used the averaged spectrum for oximetry calculation. In C57BL/6J mouse lower extremity microvasculature, their  $N_{mB}$  were approximately 60 B-scans for reliable spectral analysis, corresponding to a total time of 500 A-lines  $\times$  60 B-scans  $\times$  4 repetitions  $\times$  1.25 delay ratio / 70,000 A-lines/sec  $\approx$  2.14 s at 70 kHz A-line rate for blood vessels with sizes down to 10-15  $\mu m$ . This was the temporal resolution of the oximetry by using this protocol and data averaging, considering the microvascular  $sO_2$  can vary over time. Since the lateral resolution of vis-OCT was calculated as  $\sim 11.68 \mu m$  at 565 nm in section 2.2, the scanning speed at 70 kHz A-line rate by scanning protocol 1 was estimated by  $11.68 \mu m / (1/70 \text{ kHz} \times 500 \text{ B-scans} \times 4 \text{ repetitions} \times 1.25) \approx 0.33 \text{ mm/s}$ , which was smaller the mean flow velocity of small blood vessels ranging from 0.61 to 3.45 mm/s [31]. This indicates the validity of assuming independent blood signals from each B-scan. Under this condition, the aforementioned  $\sim 2.14$  s would correspond to a total spatial length of 1.31-7.38 mm for a similar-sized blood vessel. Therefore, in future applications,  $N_{mB}$  can be extracted from vis-OCT angiography maps without the necessity of repeated scans at the same location.

We deliberately used C57BL/6J mouse because its skin pigments / melanin could serve as intrinsic noise to test our data quality-control method with only moderate angiography SNR. We removed the effect of melanin absorption by normalizing the vessel spectrum by the spectrum of non-vascular skin tissues above this blood vessel. This was valid under the assumption that the OCT spectrum of the non-vascular tissue above the blood vessel was  $\sim \lambda^\alpha$ , as explained in section 2.7. Two main facts ensure legitimacy of this assumption. First, scattering in tissue is the result of light interacting with random variations in refractive index, thus it's reasonable to regard tissue to be comprised of a spatially random distribution of refractive index in the form of a continuous function. Under RGD scattering approximation where tissue is a weakly scattering medium, its OCT spectrum is derived to be related to  $\sim \lambda^\alpha$  [26] [27]. Second, skin melanin has a decay absorption spectrum within the oxygenation spectral range [32], favoring the assumption of  $I_t(\lambda, z_0) \propto \lambda^\alpha$ .

## 5. Conclusion

In this study, we proposed a quantitative data quality-control protocol to demonstrate *in vivo* small blood vessel vis-OCT oximetry. This quantitative protocol mainly includes extraction of OCT spectra, a three-step statistical data-cleaning process of the extracted spectra, and  $sO_2$  quantification. We validated this protocol via introducing hyperoxia for expected  $sO_2$  changes in mouse lower extremity microvasculature and conducted *in vivo* vis-OCT oximetry on C57BL/6J mouse ear microvasculature rich with small blood vessels such as capillaries. Parameters of the scanning protocols and the threshold requirements in the data-cleaning process can be flexibly adjusted according to different applications and system performance

for general applicability in the future. Therefore, the data quality-control protocol seeks to standardize the data processing method for *in vivo* oximetry in small vessels by vis-OCT. This is promising for *in vivo* backscattering-based optical oximetry such as vis-OCT to measure local capillary sO<sub>2</sub> for early diagnosis, progression monitoring, and treatment evaluation of diabetic retinopathy and cancer.

## Appendix

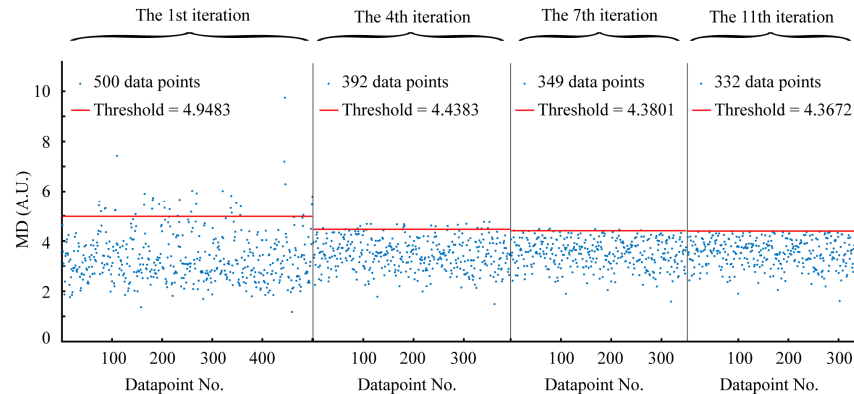


Fig. 7. Scatter plots of Vessel 1 in Fig. 3 at iterations 1, 4, 7, and 11 during the anomaly detection and outlier removal process. Red lines indicate the thresholds for the Mahalanobis distance (MD) between each repetitive spectrum of the blood vessel ( $x_i$ ) and their mean ( $\mu$ ), represented by  $\hat{d} = \mu + 1.645\sigma$ , where  $\sigma$  is variance. The values of  $\hat{d}$  at iterations 1, 4, 7, and 11 are 4.9483, 4.4383, 4.3801, and 4.3672, respectively. Blue dots above the red lines at each iteration were discarded as outliers. The number of data points with MD lower than the thresholds at iterations 1, 4, 7, and 11 are 463, 373, 340, and 332, respectively.

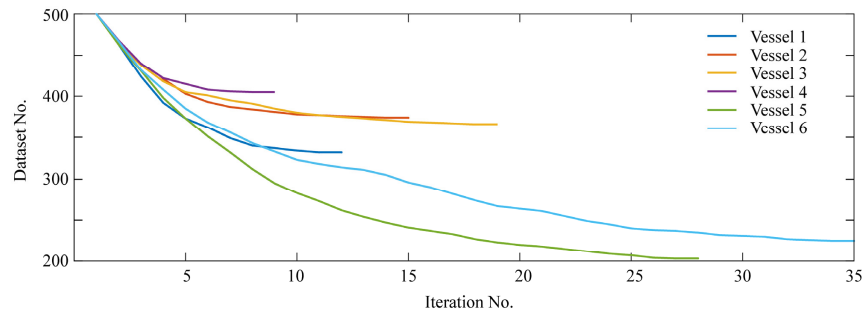


Fig. 8. The number of repetitive B-scans detected as normal at each iteration of the anomaly detection and outlier removal process for (a): Vessel 1, (b): Vessel 2, (c): Vessel 3, (d): Vessel 4, (e): Vessel 5, and (f): Vessel 6 shown in Fig. 3. The total iteration numbers of vessel 1 to vessel 6 are 12, 15, 19, 9, 28, and 35, respectively.

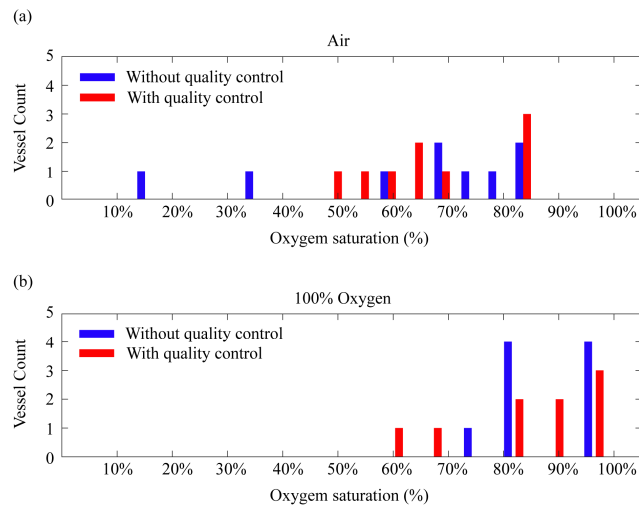


Fig. 9. The sO<sub>2</sub> histograms of blood vessels in Figs. 4(a) and (b) without and with the data-quality process at normal (a) and 100% oxygen (b) conditions.

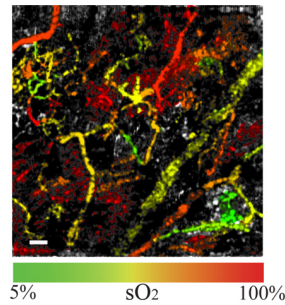


Fig. 10. The *en face* sO<sub>2</sub> map of C57BL/6J mouse ear microvasculature without data quality control process. Scale bar: 100 μm.

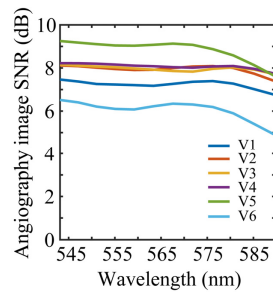


Fig. 11. The spectroscopic angiography image SNR of the six vessels marked in Figs. 3(a) and 3(b). V1-V6: Vessel 1 to Vessel 6.

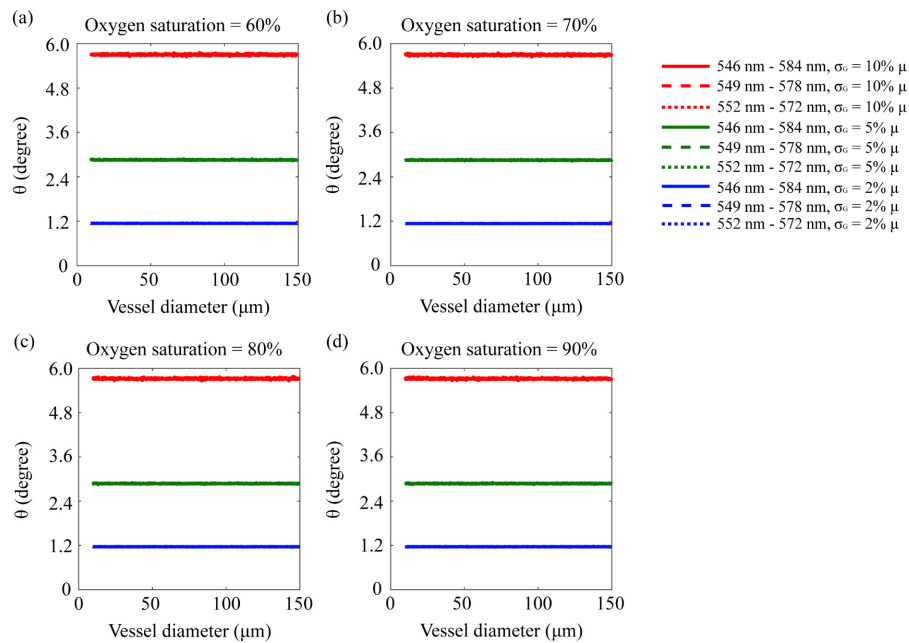


Fig. 12. The intersection angles between simulated OCT spectra with and without different zero-mean Gaussian white noise for three different spectral bands. The standard deviations ( $\sigma_G$ ) of the Gaussian white noise were approximately 10%, 5%, and 2%, respectively, of the mean of the simulated spectrum ( $\mu$ ) with  $sO_2$  as  $\alpha$ . The oxygen saturations of the simulated OCT spectra are (a): 60%, (b): 70%, (c): 80% and (d): 90%. The three spectral bands are 546 nm - 584 nm, 549 nm - 578 nm, and 552 nm - 572 nm, indicated by red, green, and blue, respectively. All curves are the mean of 100 iterations of the simulations.

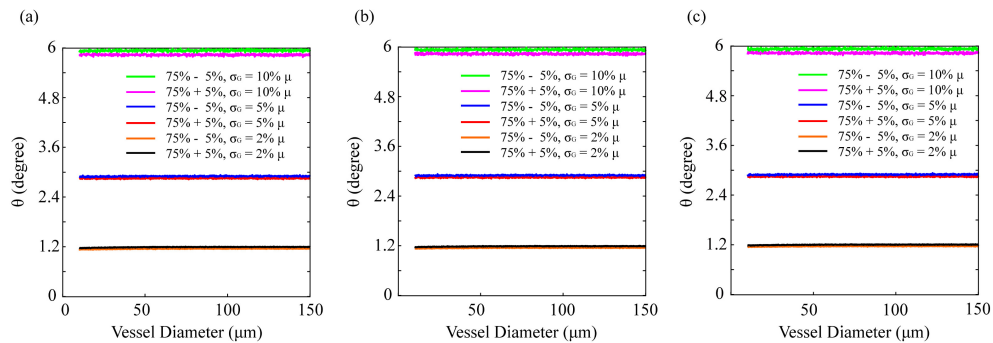


Fig. 13. The intersection angles between simulated spectra of blood vessels with  $sO_2$  as  $\alpha$  and  $\alpha \pm 5\%$  added by a zero-mean Gaussian white noise. The standard deviations ( $\sigma_G$ ) of the Gaussian white noise were approximately 10%, 5%, and 2% of the mean of the simulated spectrum ( $\mu$ ) with  $sO_2$  as  $\alpha$ . (a):  $\alpha = 60\%$ , (b):  $\alpha = 75\%$ , and (c):  $\alpha = 90\%$ . All curves are the mean of 100 iterations of the simulations.

## Funding

National Institute of Health (NIH) (R01CA183101, R01CA165309, R01CA173745); National Science Foundation (NSF) (CBET-1240416); Bright Focus foundation (G2017077); Boston University Clinical & Translational Science Institute (BU-CTSI) (1KL2TR001411); NIH/NCL (1R01CA224911-01A1).



## Acknowledgment

We thank Benjamin D. Keane for proof-readings.

## Disclosures

The authors have no relevant financial interests in this article and no potential conflicts of interest to disclose.

## References

1. E. Stefansson, "Ocular Oxygenation and the Treatment of Diabetic Retinopathy," *Surv. Ophthalmology* **51**(4), 364–380 (2006).
2. P. Vajkoczy, A. Ullrich, and M. D. Menger, "Intravital Fluorescence Videomicroscopy to Study Tumor Angiogenesis and Microcirculation," *Neoplasia* **2**(1-2), 53–61 (2000).
3. B. I. Levy, E. L. Schiffrin, J. Mourad, D. Agostini, E. Vicaut, M. E. Safar, and H. A. J. Struijker-boudier, "Impaired Tissue Perfusion A Pathology Common to Hypertension, Obesity, and Diabetes Mellitus," *Circulation* **118**(9), 968–976 (2008).
4. A. Edwards-richards, M. Defreitas, C. P. Katsou, W. Seeherunvong, N. Sasaki, M. Freundlich, G. Zilleruelo, and C. L. Abitbol, "Capillary rarefaction : an early marker of microvascular disease in young hemodialysis patients," *Clin. Kidney J.* 569–574 (2014).
5. R. N. Kalaria, "Neurodegenerative disease: Diabetes, microvascular pathology and Alzheimer disease," *Nat. Rev. Neurol.* **5**(6), 305–306 (2009).
6. J. Yi, Q. Wei, W. Liu, V. Backman, and H. F. Zhang, "Visible-light optical coherence tomography for retinal oximetry," *Opt. Lett.* **38**(11), 1796–1798 (2013).
7. J. Yi, S. Chen, V. Backman, and H. F. Zhang, "In vivo functional microangiography by visible-light optical coherence tomography," *Biomed. Opt. Express* **5**(10), 3603–3612 (2014).
8. S. Chen, J. Yi, and H. F. Zhang, "Measuring oxygen saturation in retinal and choroidal circulations in rats using visible light optical coherence tomography angiography," *Biomed. Opt. Express* **6**(8), 2840–2853 (2015).
9. S. P. Chong, C. W. Merkle, C. Leahy, H. Radhakrishnan, and V. J. Srinivasan, "Quantitative microvascular hemoglobin mapping using visible light spectroscopic Optical Coherence Tomography," *Biomed. Opt. Express* **6**(4), 1429–1450 (2015).
10. L. Kagemann, G. Wollstein, M. Wojtkowski, H. Ishikawa, K. A. Townsend, M. L. Gabriele, V. J. Srinivasan, J. G. Fujimoto, and J. S. Schuman, "Spectral oximetry assessed with high-speed ultra-high-resolution optical coherence tomography," *J. Biomed. Opt.* **12**(4), 041212 (2007).
11. R. D. Ferguson, Z. Zhong, D. X. Hammer, M. Mujat, A. H. Patel, C. Deng, W. Zou, and S. A. Burns, "Adaptive optics scanning laser ophthalmoscope with integrated wide-field retinal imaging and tracking," *J. Opt. Soc. Am. A* **27**(11), A265–A277 (2010).
12. A. Pinhas, M. Dubow, N. Shah, T. Y. Chui, D. Scoles, Y. N. Sulai, R. Weitz, J. B. Walsh, J. Carroll, A. Dubra, and R. B. Rosen, "In vivo imaging of human retinal microvasculature using adaptive optics scanning light ophthalmoscope fluorescein angiography," *Biomed. Opt. Express* **4**(8), 1305–1317 (2013).
13. R. J. Zawadzki, S. M. Jones, S. Pilli, S. Balderas-Mata, D. Y. Kim, S. S. Olivier, and J. S. Werner, "Integrated adaptive optics optical coherence tomography and adaptive optics scanning laser ophthalmoscope system for simultaneous cellular resolution in vivo retinal imaging," *Biomed. Opt. Express* **2**(6), 1674–1686 (2011).
14. T. Y. P. Chui, D. A. Vannasdale, and S. A. Burns, "The use of forward scatter to improve retinal vascular imaging with an adaptive optics scanning laser ophthalmoscope," *Biomed. Opt. Express* **3**(10), 2537–2549 (2012).
15. L. Wang, K. Maslov, and L. V. Wang, "Single-cell label-free photoacoustic flowoxigraphy in vivo," *PNAS* **110**, 5759–5764 (2013).
16. J. Yi, W. Liu, S. Chen, V. Backman, N. Sheibani, C. M. Sorenson, A. A. Fawzi, R. A. Linsenmeier, and H. F. Zhang, "Visible light optical coherence tomography measures retinal oxygen metabolic response to systemic oxygenation," *Light Sci. Appl.* **3**, 1–10 (2015).
17. X. Shu, L. Beckmann, and H. Zhang, "Visible-light optical coherence tomography: a review," *J. Biomed. Opt.* **22**(12), 1–14 (2017).
18. R. Liu, G. Spicer, S. Chen, H. F. Zhang, J. Yi, and V. Backman, "Theoretical model for optical oximetry at the capillary level: exploring hemoglobin oxygen saturation through backscattering of single red blood cells," *J. Biomed. Opt.* **22**(2), 025002 (2017).
19. R. Liu, J. A. Winkelmann, G. Spicer, Y. Zhu, A. Eid, G. A. Ameer, V. Backman, and J. Yi, "Single capillary oximetry and tissue ultrastructural sensing by dual-band dual-scan inverse spectroscopic optical coherence tomography," *Light Sci. Appl.* **7**(1), 57 (2018).
20. W. Song, L. Zhou, S. Zhang, S. Ness, D. Manishi, and Y. Ji, "Fiber-based visible and near infrared optical coherence tomography (vnOCT) enables quantitative elastic light scattering spectroscopy in human retina," *Biomed. Opt. Express* **9**(7), 3464–3480 (2018).
21. L. Scolaro, R. A. McLaughlin, B. R. Klyen, B. A. Wood, P. D. Robbins, C. M. Saunders, S. L. Jacques, and D. D. Sampson, "Parametric imaging of the local attenuation coefficient in human axillary lymph nodes assessed using

- optical coherence tomography,” Biomed. Opt. Express **3** (2), 1122–1128 (2012).
22. D. J. Faber, E. G. Mik, M. C. G. Aalders, and T. G. van Leeuwen, “Light absorption of (oxy-)hemoglobin assessed by spectroscopic optical coherence tomography,” Opt. Lett. **28**(16), 1436–1438 (2003).
  23. L. Zhang, W. Song, D. Shao, S. Zhang, M. Desai, S. Ness, S. Roy, and J. Yi, “Volumetric fluorescence retinal imaging *in vivo* over a 30-degree field of view by oblique scanning laser ophthalmoscopy (oSLO),” Biomed. Opt. Express **9**(1), 25–40 (2017).
  24. W. Song, L. Zhou, K. L. Kot, H. Fan, J. Han, and J. Yi, “Measurement of flow-mediated dilation of mouse femoral artery *in vivo* by optical coherence tomography,” J. Biophotonics **5**, 1–9 (2018).
  25. Y. Jia, O. Tan, J. Tokayer, B. Potsaid, Y. Wang, J. Jonathan, M. F. Kraus, H. Subhash, J. G. Fujimoto, J. Hornegger, and D. Huang, “Split-spectrum amplitude-decorrelation angiography with optical coherence tomography,” Opt. Express **20**(4), 3116–3121 (2012).
  26. J. D. Rogers, A. J. Radosevich, J. Yi, and V. Backman, “Modeling light scattering in tissue as continuous random media using a versatile refractive index correlation function,” IEEE J. Sel. Top. Quantum Electron. **20**(2), 7000514 (2013).
  27. J. Yi, A. J. Radosevich, J. D. Rogers, S. C. P. Norris, İ. R. Çapoğlu, A. Taflove, and V. Backman, “Can OCT be sensitive to nanoscale structural alterations in biological tissue?” Opt. Express **21**(7), 9043–9059 (2013).
  28. Y. Wang, H. Song, K. Maslov, Z. Yu, X. Younan, and W. Lihong V., “In vivo integrated photoacoustic and confocal microscopy of hemoglobin oxygen saturation and oxygen partial pressure,” Opt. Lett. **141**(4), 520–529 (2008).
  29. F. E. Robles, S. Chowdhury, and A. Wax, “Assessing hemoglobin concentration using spectroscopic optical coherence tomography for feasibility of tissue diagnostics,” Biomed. Opt. Express **1**(1), 310–317 (2010).
  30. F. E. Robles, C. Wilson, G. Grant, and A. Wax, “Molecular imaging true-colour spectroscopic optical coherence tomography,” Nat. Photonics **5**(12), 744–747 (2011).
  31. M. Unekawa, M. Tomita, Y. Tomita, H. Toriumi, K. Miyaki, and N. Suzuki, “RBC velocities in single capillaries of mouse and rat brains are the same, despite 10-fold difference in body size,” Brain Res. **1320**, 69–73 (2010).
  32. G. Zonios, J. Bykowski, and N. Kollias, “Skin melanin, hemoglobin, and light scattering properties can be quantitatively assessed *in vivo* using diffuse reflectance spectroscopy,” J. Invest. Dermatol. **117**(6), 1452–1457 (2001).